International Journal of
Georesources and Environment
http://ijge.camdemia.ca, ijge@camdemia.ca
IJGE 2017 3(4): 111-117
Available at http://ojs.library.dal.ca/ijge
Section – Geohazards and Environment

CO_2 Sequestration Safety Monitoring by using Seismic Imaging and Double Difference Tomography

Enji Sun[1]*, Erik Westman[2], Ben Fahrman[2] and Xu Ma[2]
[1] China Academy of Safety Science and Technology, Beijing, China
[2] Department of Mining and Mineral Engineering, Virginia Tech, Blacksburg, VA, USA

Abstract: Shale gas has become an increasingly important clean energy, which has been explored worldwide in recent decades. In the shale gas production, supercritical CO_2 acts as a fracturing fluid. For preventing any kinds of leakage of the injected supercritical CO_2, it is essential to monitor the stability of its storage hundreds of kilometres beneath the Earth's surface. Seismic tomography is an imaging technique that uses induced seismic waves to create three dimensional images of the subsurface. It is an effective monitoring method to evaluate the caprock integrity in the CO_2 sequestration storage (CCS). In this experimental research, a simulated uniaxial compressive load was applied on a granite sample to analyze the stress redistribution for long-term in-situ caprock integrity during CO_2 injection. The induced seismic waves were recorded, and seismic events were located according to the Geiger algorithm. The frequency of seismic events correlates with the caprock failure evolution. Based on the frequency of seismic events and the failure process, the seismic data is divided into four regimes to examine the failure evolution. Finally, the double difference tomography (TomoDD) algorithm using arrival time was adopted to recalculate to modify the locations of seismic events and velocity structure in each regime. The results indicate that the passive seismic system can map the caprock stress distribution and allow for imaging of the caprock integrity. TomoDD exhibits sound improvements to relocate seismic events both in relative and absolute locations as well as to characterize the local velocity structure. The study further reveals that seismic monitoring along with TomoDD could evaluate the caprock failure accurately in the CCS.

Keywords: shale gas, CO_2 sequestration storage, seismic monitoring, TomoDD, stress redistribution, caprock integrity

1 Introduction

To reduce the CO_2 concentration in the atmosphere, CO_2 capture and sequestration (CCS) has been suggested as a means of continuing to use fossil fuel resources while offsetting their negative environmental impacts (Eiken et al 2011). A positive CCS project should retain 99% of the injected supercritical CO_2 (pressure is greater than 7.38 MPa and temperature is above 31.04°C and a density is of about 700 kg/m^3) over at least 100 years (Davidson et al 2005). As large quantities of supercritical CO_2 are being injected into full scale storage, caprock stress is redistributing and the leakage could occur anywhere over a wide storage area (Hou et al 2012). Acoustic waves are emitted from the caprock, which is fractured due to the CO_2 injection that can be detected by passive seismic sensors (Shitashima et al 2013). Tomography techniques are advantageous for imaging the integrity of the caprock in the CCS projects. Velocity tomography uses waves to model entities based on the arrival time of waves (Westman et al 2001, Westman 2004, Luxbacher et al 2008). Seismic tomography is a data inference technique that exploits information contained in seismic records to constrain 2D or 3D models of the Earth's interior. It generally requires the solution of a large inverse problem to obtain a heterogeneous seismic model that is consistent with field observations (Kudryavtsev et al 2012).

To simulate the caprock stress distribution that can occur at a potential underground storage site, a uniaxial compression experiment was performed on the granite sample. The sample failure process was recorded, at the same time, the seismic data was collected and analyzed. The double difference tomography algorithm (TomoDD) was applied to perform the seismic event relocation and velocity structure modification.

2 Experiment Design and Failure Results

2.1 Experiment design and system configuration

A granite sample is prepared in a size of 204 mm × 51 mm × 32 mm. Passive seismic sensors are mounted on the sample to observe the induced elastic waves. The sample is placed on the platform of the MTS810 compressive testing system, where a constant uniaxial compressive load rate is applied to the granite sample until its failure. The force and displacement data are documented in the MTS control center

* Corresponding Author: Enji SUN, enjisun@gmail.com, phone: +86 10-8491-6615

DOI: 10.15273/ijge.2017.04.012

server. After amplification and filtering, the signals from the sensors are transmitted to the ESG seismic monitoring system. The locations of seismic events are determined based on the sensor's locations, the signal's arrival time and the velocity of compressive waves. The experimental arrangement is schematically displayed in Figure 1.

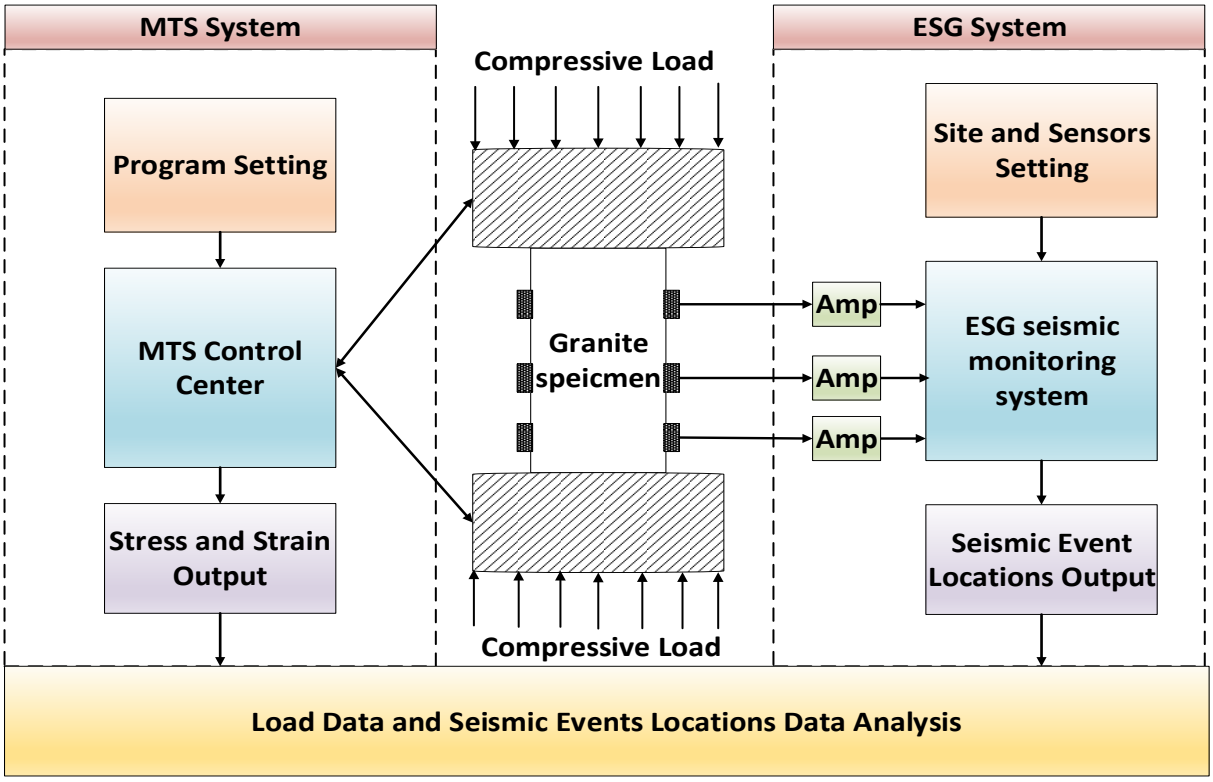

Figure 1. Experimental system for measurement of seismic event location

The level calibration of absolute displacement (the maximum displacement of compressive load) is 1.52 mm and the uniaxial compressive load period is set up to 43,200 seconds in the MTS control software. Therefore, the constant compressive load rate is 3.53e – 5 mm/s. The applied load and stroke position are monitored by the MTS system and then the force versus stroke position curve is plotted. The compressive load data is saved into the MTS server for further analysis. When the force reaches the peak load, the MTS holds the peak load level to avoid an instant pressure drop. In this experiment, the seismic monitoring system is composed of the passive seismic sensors and ESG monitoring software. Alpha R6 physical acoustic uniaxial geophones, with a range from 35 kHz to 100 kHz operating frequency and 75 dB peak sensitivity, are installed on the surface of the granite sample. The arrangement of the sensors plays an important role in a seismic monitoring network. All the surfaces of the sample are polished in order that the super glue has a better footing with the sensors. If top surface of the sample is assumed as zero level, twelve sensors are attached on the samples with -50 mm, -100 mm and -150 mm levels.

Before the configuration of the ESG software, the origin of the local coordinate system is defined at the left-lower corner on top surface of the sample. The direction that extends from left-lower corner to right-lower corner is defined as the East on the top surface. The North direction is perpendicular to the East on the top surface. The Depth is vertical with the top surface of the sample and increases downward.

2.2 Sample failure results and frequency of the seismic events

After 36,053 seconds (10.01 hour) of uniaxial compressive load, the peak load reaches 166.1 kN with 1.27 mm displacement. The granite sample fails after 36,180 seconds (10.05 hour) of continuing compressive load. Three significant brittle failures occur before the ultimate failure. The passive seismic sensors record the seismic wave's arrival time during the load acting on the sample. A total of 842 seismic events are positioned by the ESG system using Geiger algorithm (Geiger 1912). Seismic events occur in a lower event frequency before the compressive load reaches the peak value. The seismic events are triggered when the microcracks coalescence or failure occurs inside of the sample. Some insignificant cracks are observed at the location of 30 mm east, 60 mm depth. No rock failure is found before the peak load. The frequency of the seismic events is plotted with the force versus displacement curve in Figure 2.

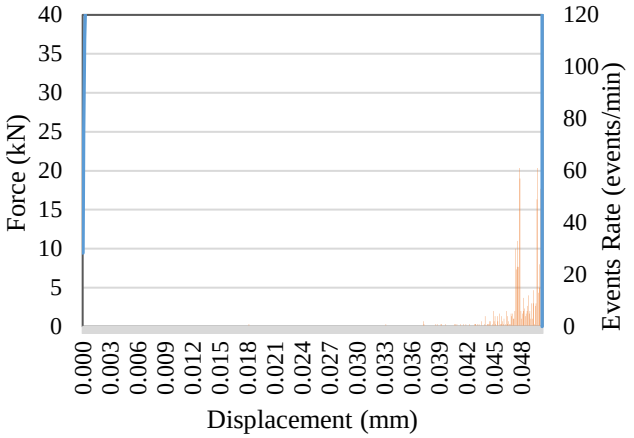

Figure 2. Force and displacement curve with seismic event occurrence frequency plot

The shear failure occurs concurrently with a high frequency of the seismic events as the compressive load is close to the peak value. Three significant rock failures take place during the process that coincides with the increment of seismic events frequency. The first major failure occurs at the peak load with a frequency of 61 events/min, the second failure occurs after the peak load with a frequency at 53 events/min, and the seismic events rate is 113 events/min during the last one.

3 Double Difference Seismic Tomography Calculation and Velocity Structure Analysis

3.1 Failure procedure division and seismic event locations

The seismic data is divided into four regimes based on the frequency of seismic events and failure process (Figure 3). The 1st regime (R1) starts from the beginning to the moment of first peak frequency of events. Regime 2 (R2) starts when the event frequency decreases and ends prior to the moment of the second peak frequency of events. Regime 3 (R3) is when the sample reaches the peak compressive load and begins to approach failure. Regime 4 (R4) includes the data at failure and post failure.

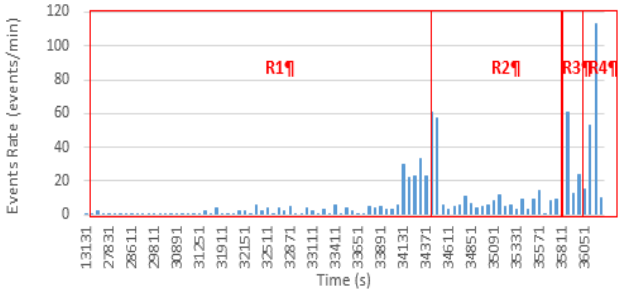

Figure 3. The data with four regimes divided based on the frequency of seismic events

R1, R2 and R3 are in the ascending period of compressive load. The load keeps increasing at a constant rate in these regimes. The last regime is in the post peak load period as the failures happened. The detailed regime's separation and seismic event distribution are exhibited in Table 1.

Table 1. Regime's separation and seismic events distribution

Regime ID	Load time(s)	Peak event frequency	Number of seismic events
R1	0 ~ 34,371	33	246
R2	34,372 ~ 35,751	61	258
R3	35,752 ~ 36,051	61	162
R4	36,052 ~ 36,181	113	176

The distribution of seismic event locations in different regimes in a view from the left is displayed in Figure 4. In R1, as the compressive load increases, the seismic events concentrate on 20 mm in the north direction and 40 mm in depth direction. The majority of the events are located at 50 mm depth after the post peak load in R4.

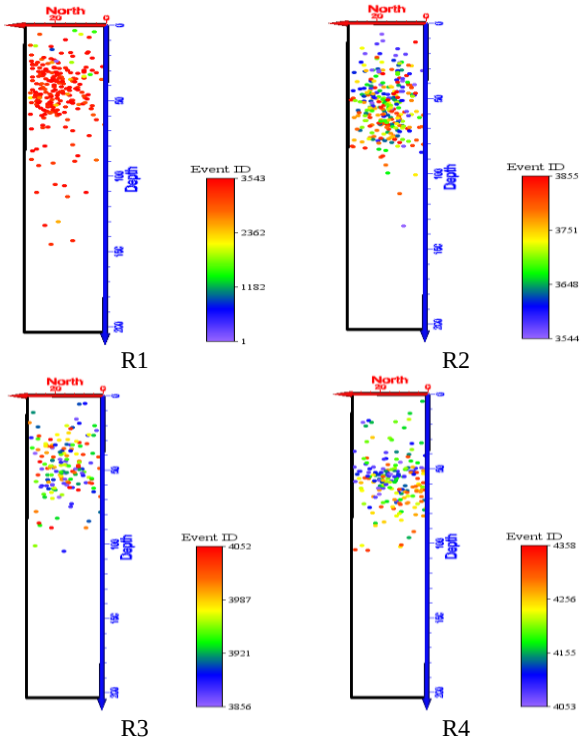

Figure 4. The distribution of seismic event locations in different regimes in a view from the left

The distribution of seismic event locations in different regimes in a view from the front is presented in Figure 5. The seismic events aggregate at 40 mm in the east direction in R1. The events distribute in the center of the sample in R2. Then the majority events are located at 20 mm in the east direction before the peak load. At R4, most events are located at 50 mm depth.

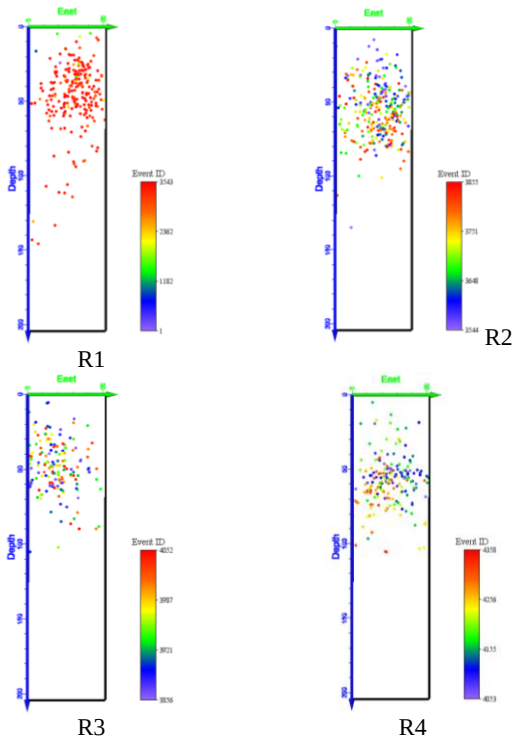

Figure 5. The distribution of seismic event locations in different regimes in a view from the front

Figure 6 shows the distribution of the seismic event locations in a view from the top. The events concentrate at 25 mm in the north direction and 40 mm in the east direction in R1. The density of events cluster at 20 mm in the north direction and 20 mm in the east direction in R3. The events are kind of scattering after the peak load in R4.

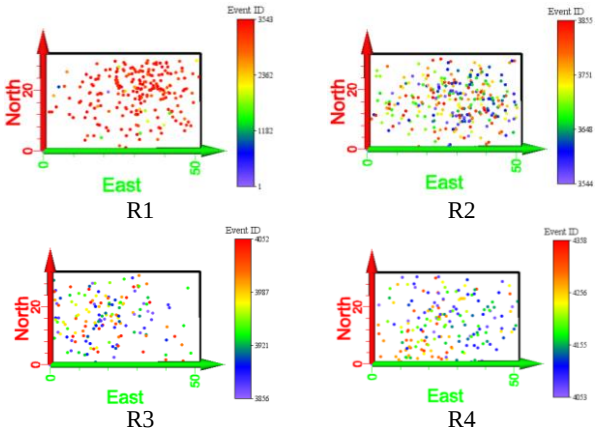

Figure 6. The distribution of seismic event locations in different regimes in a view from the top

3.2 Double difference seismic tomography calculation and velocity model construction

The locations of seismic events are somewhat scattered in the east direction, as mentioned above. The double difference (DD) seismic location algorithm is used to relocate seismic events in the presence of measurement errors and model uncertainty (Zhang and Thurber 2003).

In the double-difference relocation algorithm, the arrival time T from a seismic event i to a sensor station k is expressed as:

$$T_k^i = \tau^i + \int_i^k u\, ds \qquad (1)$$

In this equation, $\tau^i$is the origin time of event i , u is the slowness field, and ds is an element of path length.

dr_k^{ij} is the residual between observed and calculated differential travel time between the two events defined as double-difference equation (Waldhauser and Ellsworth 2000, Waldhauser 2001):

$$dr_k^{ij} = (t_k^i - t_k^j)^{obs} - (t_k^i - t_k^j)^{cal} \qquad (2)$$

The tomoDD identifies events that can make an event pair, and categorizes the station or stations that each pair can be linked to in order to make travel time corrections to that station (Zhang and Thurber 2003, 2006). Ultimately the event pairs are grouped together in clusters and the least squares solution for each cluster is found to achieve relative locations.

The relocated seismic events show fewer events than the original ones. The events around 20 mm in the north direction and 50 mm in the depth direction are more densely clustered after the relocation processing. The events are relocated at 15 mm in the north direction in R2 and R3 before the peak load. A few events are located at 10 mm in the north direction in R4. The distribution of relocated seismic event in different regimes in a view from the left is depicted in Figure 7.

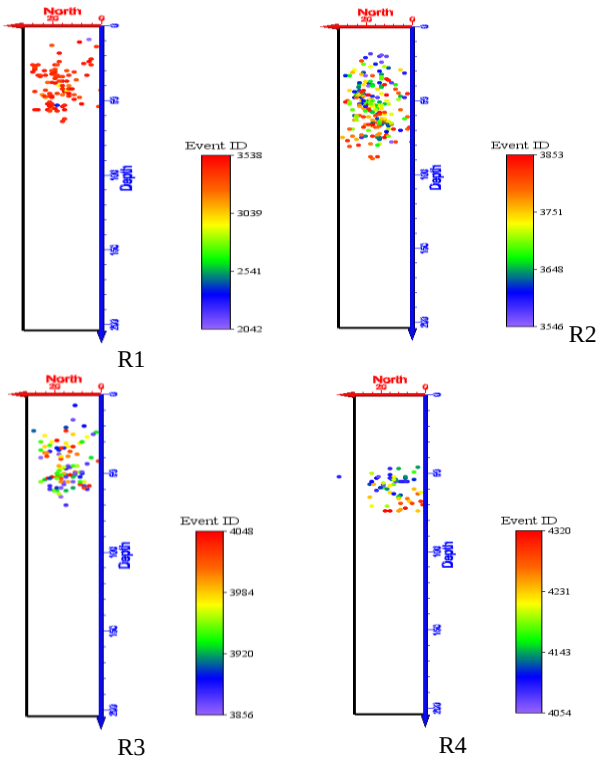

Figure 7. The distribution of relocated seismic event in different regimes in a view from the left

The distribution of relocated seismic event in different regimes in a view from the front is shown in Figure 8. The event relocations of R1 are clustered at 50 mm in the depth direction. As the compressive load increases, the events of R2 cluster around 50 mm in the depth direction. The events relocate at 20 mm in the east direction before the peak load in R3. R4 shows the events gather at 50 mm in the depth direction.

The high velocity zones are located at 22 mm in the north direction in R1. Due to the anisotropic parameters of the granite sample, the high velocity zones expand and occur at 30 mm in the east.

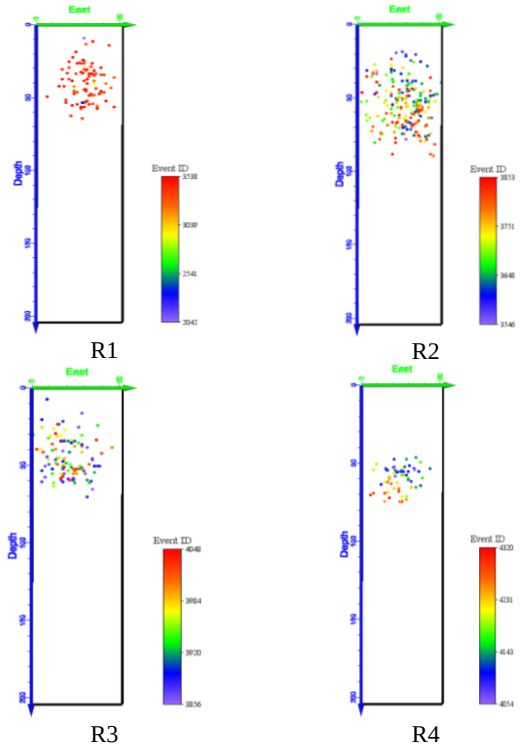

Figure 8. The distribution of seismic event relocations in different regimes in a view from the front

The relocated seismic event distribution of different regimes in a view from the top is presented in Figure 9. The event relocations occur at 20 mm in the north direction and 40 mm in the east direction in R1. As load increases, the event distribution is kind of scattering in the east direction in R2. The events cluster at 25 mm in the east direction in R3 before the peak load. A few events are relocated at 25 mm in the east direction in R4 after the peak load.

18 mm in the north direction and at a depth of 50 mm in R2. The high velocity zones are located at 25 mm in the north direction in R3 at the peak load. After three major failures, the high velocity zones are much smaller in R4. Orthogonal image of velocity structure of different regimes in a view from the right is shown in Figure 10.

Orthogonal image of velocity structure of different regimes in a view from the front is displayed in Figure 11. The high velocity zones are located at 40 mm in the east direction and 50 mm in depth direction in R1. As the

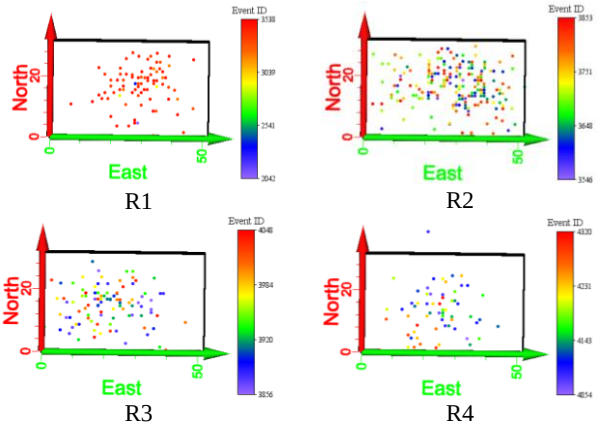

Figure 9. The relocated seismic event distribution of different regimes in a view from the top

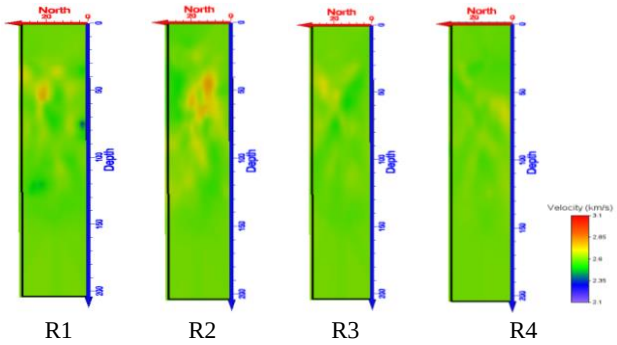

Figure 10. Orthogonal image of velocity structure of different regimes in a view from the right

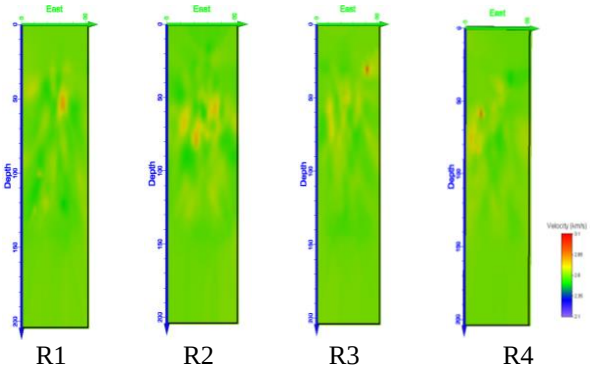

Figure 11. Orthogonal image of velocity structure of different regimes in a view from the front

compressive load increases, the high velocity zones expand in the east direction and lie in the deeper positions in R2. The high velocity zones concentrate at 40 mm in the east direction and at 40 mm depth. They extend from 30 mm to 80 mm in the depth direction in R3. The high velocity zones are located at 20 mm in the east direction and 90 mm in the depth direction.

Orthogonal image of velocity structure of different regimes in a view from the top is presented in Figure 12. The high velocity zones first gather at 25 mm in the north direction and 30 mm in the east direction in R1. Then they

expand to 15mm in the north direction and 15 mm in the east direction. The high velocity zones reduce a lot after the failure in R4.

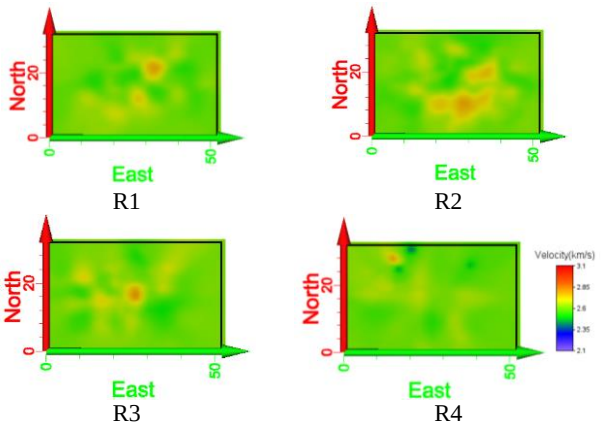

Figure 12. Orthogonal image of velocity structure of different regimes in a view from the right

4 Conclusions

In this experimental research, a simulated uniaxial compressive load was applied on the granite sample to analyze the stress redistribution for long-term in-situ caprock integrity during the CO_2 injection. The induced seismic waves were recorded to trace seismic events based on the Geiger algorithm. The frequency of seismic events was correlated with the caprock failure evolution. The acquired seismic data was divided into four regimes according to the frequency of seismic events and failure process to examine the failure evolution. Furthermore, the double difference tomography (TomoDD) algorithm was adopted to recalculate the locations of seismic events and velocity structure in each regime by using arrival time.

The results indicate that the passive seismic system can map the caprock stress distribution and allow for imaging of the caprock integrity. Tomography provides a visual representation of the stress distribution beneath the surface, allowing for non-intrusive imaging of the rock mass. TomoDD has the ability to relocate the seismic events both in relative and absolute locations, as well as characterizing the local velocity structure. The study reveals that seismic monitoring along with TomoDD could evaluate the caprock failure accurately in the CCS, which could improve the sustainable development in the minerals industry.

Acknowledgement

We sincerely thank all the members of the Geomechanics Observation and Imaging (GOI) from Virginia Tech for their insights and helpful comments on this paper. This work has been sponsored by the National Energy Technology Laboratory (NETL) and performed under the auspices of the U.S. Department of Energy (DOE) under contract 4000.4.641.061.001.531. This work is also supported by National Natural Science Foundation of China (71373245, 50974109), the basic research funding of China Academy of Safety Science and Technology (2016JBKY07), National Key Research & Development program (2017YFC0805107, 2016YFC0801305).

References

Davidson, B.M.O., H.C. de Coninck, M. Loos and L.A. Mayer, 2005. IPCC Special Report on CO_2 Capture and Storage. Prepared by Working Group III of the International Panel on Climate Change. Cambridge University Press.

Eiken, O., P. Ringrose, C. Hermanrud, B. Nazarian, T.A. Torp and L. Høier, 2011. Lessons learned from 14 years of CCS operations: Sleipner, In Salah and Snøhvit. Energy Procedia, **4**: 5541 - 5548. DOI: 10.1016/j.egypro.2011.02.541.

Geiger, L., 1912. Probability method for the determination of earthquake epicenters from the arrival time only. Bull. St. Louis Univ, **8**: 60 - 71.

Hou, Z., M.L. Rockhold and C.J. Murray, 2012. Evaluating the impact of caprock and reservoir properties on potential risk of CO_2 leakage after injection. Environmental Earth Sciences, **66**(**8**): 2403 - 2415. DOI: 10.1007/s12665-011-1465-2.

Kudryavtsev, V. A., N. J. C. Spooner, J. Gluyas, C. Fung and M. Coleman, 2012. Monitoring subsurface CO_2 emplacement and security of storage using muon tomography. International Journal of Greenhouse Gas Control, **11:** 21 - 24. DOI: 10.1016/j.ijggc.2012.07.023.

Luxbacher, K., E. Westman, P. Swanson and M. Karfakis, 2008. Three-dimensional time-lapse velocity tomography of an underground longwall panel. International Journal of Rock Mechanics and Mining Sciences, **45**(**4**): 478 - 485. DOI: 10.1016/j.ijrmms.2007.07.015.

Shitashima, K., Y. Maeda and T. Ohsumi, 2013. Development of detection and monitoring techniques of CO_2 leakage from seafloor in sub-seabed CO_2 storage. Applied Geochemistry, **30**: 114 - 124. DOI: 10.1016/j.apgeochem.2012.08.001.

Waldhauser, F., 2001. hypoDD – A Program to Compute Double-Difference Hypocenter Locations. U.S. Geological Survey, Open File Report, **01-113**: 1 - 25.

Waldhauser, F. and W.L. Ellsworth, 2000. A double-difference earthquake location algorithm: method and application to the Northern Hayward Fault, California. Bulletin of the Seismological Society of America, **90**(**6**): 1353 - 1368. DOI: 10.1785/0120000006.

Westman, E., 2004. Use of tomography for inference of stress redistribution in rock. IEEE Transactions on Industry Applications, **40(5)**: 1413 - 1417. DOI: 10.1109/IAS.2003.1257776.

Westman, E., K.A. Heasley, P.L. Swanson and S. Paterson, 2001. A correlation between seismic tomography, seismic events and support pressure. In Proc. 38th Rock Mechanics Symp., Washington, DC: 319 - 326.

Zhang, H. and C.H. Thurber, 2003. Double-difference tomography: The method and its application to the Hayward Fault, California. Bulletin of the Seismological

Society of America, **93**(**5**): 1875 - 1889. DOI: 10.1785/0120020190.

Zhang, H. and C. Thurber, 2006. Development and applications of double-difference seismic tomography. Pure and applied geophysics, **163**(**2-3**): 373 - 403. DOI: 10.1007/s00024-005-0021-y.